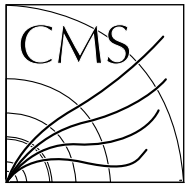

The Compact Muon Solenoid Experiment

CMS Note

Mailing address: CMS CERN, CH-1211 GENEVA 23, Switzerland

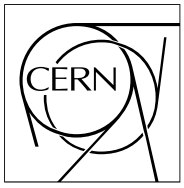

18/12/2006

Saturation and energy corrections for TeV electrons and photons

B. Clerbaux, Sh. Elgammal, T. Mahmoud, P. Marage

ULB, Université Libre de Bruxelles, Brussels, Belgium

Abstract

This note presents a study of the response of the CMS electromagnetic calorimeter ECAL to high energy electrons and photons (from 500 to 4000 GeV), using the full simulation of the CMS detector. The longitudinal containment and the lateral extension of high energy showers are discussed, and energy and η dependent correction factors $F_{\rm cor}(E_{\rm meas}, \eta)$, where $E_{\rm meas} = E_{\rm ECAL} + E_{\rm HCAL}$, are determined in order to reconstruct the incident particle energy, using the energies measured in the ECAL and in the hadronic calorimeter HCAL. For ECAL barrel crystals with energy deposit higher than 1700 GeV, improvements are proposed to techniques aimed at correcting for the effects of electronics saturation.

1 Introduction

One of the main programs of the CMS experiment is the search for new physics beyond the Standard Model, in particular the discovery of heavy resonances which subsequently decay into very energetic particles. The electron and photon decay channels are particularly promising [1, 2], due to the excellent performance of the electromagnetic calorimeter ECAL.

The ECAL consists in nearly 80 000 $\mathrm{PbWO_4}$ crystals, corresponding to at least 25 radiation lengths and 1 Moliere radius. The incident particle energy is reconstructed using the signals collected in crystals dynamically grouped into clusters.

The calibration of the cluster algorithms and corrections for energy losses due to the presence of material in front of the ECAL have been studied for electrons and photons with transverse energies less than about 100 GeV [3]. However different effects come into play at higher energies. The object of this note is to study the various effects contributing to energy losses at high energy, and to determine correction factors to be applied to the measurements in the ECAL and the HCAL, in order to reconstruct the incident particle energy. These correction factors, which are energy and η dependent, are determined for electrons and photons with energies in the range 500 to 4000 GeV.

It is known, however, that the ECAL readout electronics saturates at about 1.7 TeV in the barrel, and 3.0 TeV in the endcaps [4]. Very high energy electromagnetic showers which deposit this much energy in a single crystal thus need to be reconstructed in a way that takes account of this saturation. In this note, we present the results of further studies and improvements to the techniques presented in Ref. [5].

Nine calibration samples of electrons and photons with fixed energies, $E \geq 500$ GeV, and uniform η distributions up to $|\eta| = 2.5$ were generated using detailed simulation programs of the CMS detector (versions 365 of OSCAR and 873 of ORCA [6]). The primary vertex positions were distributed along the z-axis according to the LHC expectation.

Section 2 gives an overview of the ECAL structure and relevant characteristics, and describes the clustering algorithms. The characteristics of the energy fraction measured in the ECAL are studied in Section 3. Sections 4 and 5 discuss energy losses due to the longitudinal shower containment and to the lateral shower extension and Bremsstrahlung effects, respectively. Section 6 is devoted to the determination of the $F_{\mathrm{cor}}(E, \eta)$ correction factors, for electron and photon energies from 500 to 2000 GeV in the barrel and up to 4000 GeV in the endcaps. For energies above 2000 GeV in the barrel, where saturation occurs, Section 7.1 presents improvements to the saturation correction function of Ref. [5], and the determination of the $F_{\mathrm{cor}}(E, \eta)$ factors is performed in Section 7.2. Summary and conclusions are presented in the last Section.

2 The CMS electromagnetic calorimeter

The CMS electromagnetic calorimeter ECAL and its performance are presented in Refs. [7, 8]. The ECAL calorimeter is divided in a barrel section (EB) and two endcaps (EE), as shown in Fig. 1. The excellent linearity between the energy deposited by electromagnetic showers and the measured electronics signals, as determined

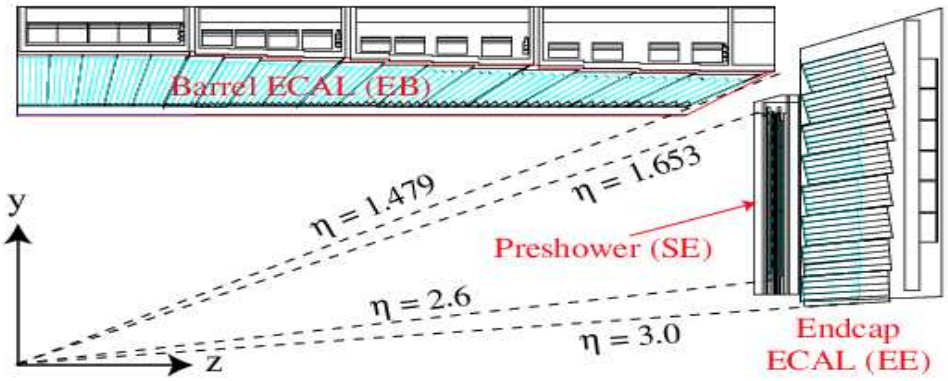

Figure 1: Longitudinal view of one quarter of the ECAL [3].

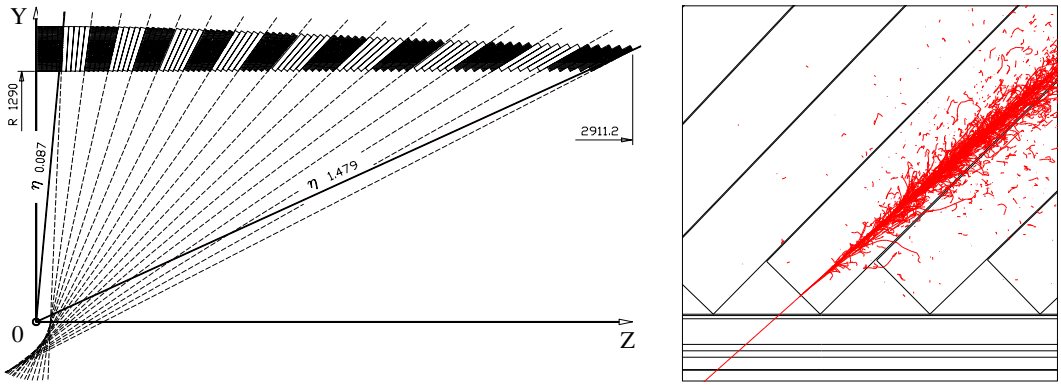

Figure 2: Off-pointing of ECAL crystals and effect on shower containment [7].

through calibration procedures, is expected to lead to an energy resolution given by a quadratic sum of terms: $\sigma/E = 0.55\% \oplus 2.7\%/\sqrt{E} \oplus 0.155/E$ in EB for $\eta = 0$, and $\sigma/E = 0.55\% \oplus 5.7\%/\sqrt{E} \oplus 0.205/E$ in EE for $\eta = 2$, with E in GeV [7]. At high energy, the constant term dominates, and the energy resolution is expected to be $\simeq 0.6\%$.

2.1 ECAL geometry

The ECAL consists of 75848 $PbWO_4$ crystals, with density $\rho = 8.3$ g/cm^3, radiation length $X_0 = 0.89$ cm and Moliere radius $r_M = 2.19$ cm. The crystals are positioned according to a quasi-projective geometry toward the nominal interaction point, with additional off-pointings intended at reducing the effects of cracks (see Fig. 2). The off-pointings are of 3° in the azimuthal (ϕ) direction (with an additional off-set of 15.9 mm below the beam direction), and of 3° in the polar (θ) direction for the barrel and 2 to 5° for the endcaps.

The barrel covers the rapidity region $|\eta| \lesssim 1.479$ ($\theta = 25.6°$). It is divided in two halves, consisting of 18 supermodules, each of which covers 20° in ϕ. Each supermodule is divided in four modules, and each module is made of four towers of five crystals (five towers for the first module), as shown in Fig. 1. The gaps (in η and in ϕ) between modules are of ~ 6 mm. The 61200 EB crystals have truncated pyramidal shapes (17 types in total to ensure complete coverage) with (approximately) squared $\sim 2.2 \times 2.2$ cm^2 front faces, which corresponds to widths in ϕ of $\sim 1° \simeq 0.0174$ rad and in η of ~ 0.0174, nearly constant over the whole EB length. The crystal lateral extensions correspond to about 1 r_M. The crystal length in the EB is 230 mm, i.e. 25.8 X_0. The centres of the crystal front faces are lying at a radius $R = 1.29$ m of the beam axis.

The endcaps, situated at 3.21 m of the nominal interaction point, extend the angular coverage to $|\eta| \lesssim 3.0$ ($\theta = 5.7°$). Each is made of two D-shape structures, where the crystals are distributed in a $x - y$ grid. The 14648 EE crystals have a nearly parallelepipedal shape, with $\sim 2.47 \times 2.47$ cm^2 front faces and length 220 mm, i.e. 24.7 X_0. In front of most of the endcaps, Pb–Si preshower calorimeters cover $1.653 \leq |\eta| \leq 2.6$ (i.e. radii 123 cm $\geq$ R $\geq$ 45 cm from the beam axis). Their material content corresponds to 3 X_0. In the following, the preshowers will be treated as part of the EE, and the energy collected in the preshowers included in the EE energy measurement.

The ECAL calorimeter is surrounding the tracker, and is inserted into the hadronic calorimeter HCAL. The material budget in front of the ECAL crystals, due to beam pipe, tracker, cables and supports, varies with η from a minimum of 0.35 X_0 at $\eta = 0$ to a maximum of 1.4 X_0 for $|\eta| \simeq 1.6$, with 0.8 X_0 for $|\eta| = 2.5$ (see Fig. 3(a)). The amount of material between the ECAL and the HCAL, due to the presence of the ECAL electronics, cooling, cables and supports, corresponds to about $3X_0$ in average (see Fig. 3(b)).

The transition region between EB and EE, $1.442 < |\eta| < 1.566$, which is shadowed by a large amount of tracker cables, and the region of EE closest to the beams, $|\eta| > 2.5$, with poor measurement precision, are not considered in this note.

2.2 Clustering and superclustering algorithms

The energy deposited in the ECAL calorimeter by electron or photon showers, E_{ECAL}, is determined – on basis of the collected electronics signals – using pattern reconstruction procedures which aim at determining the true

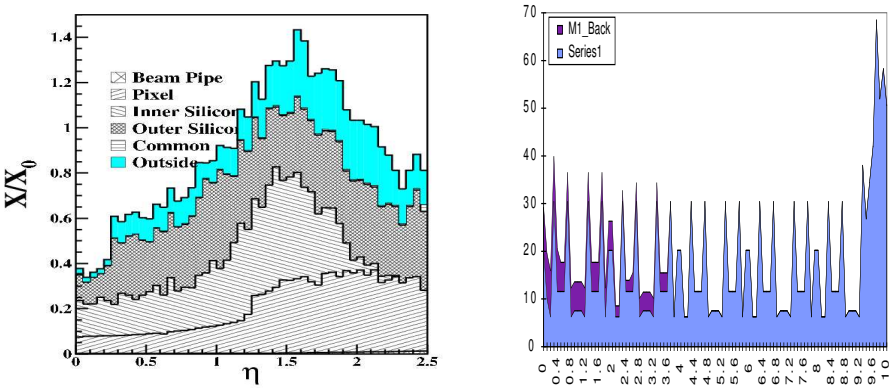

(a) (b)

Figure 3: (a) Material budget in front of the ECAL, as a function of $|\eta|$ [3]; (b) ECAL material budget in front of the HCAL, for one of the four module types [7]. The horizontal scale spans one half of a supermodule in ϕ (°). The vertical scale is in % of one interaction length λ, with $0.1\ \lambda \simeq 2.5\ X_0$.

incident particle energy. In the following, the CMS standard algorithms are used: the *Hybrid algorithm* in the barrel region and the *Island algorithm* for the endcaps (Refs. [3, 9]) [1)].

Local maxima ("seeds") in energy deposit above some threshold are identified, to which neighboring cells with monotonically decreasing energies are joint as long as they contain an energy deposit significantly higher than the background (60 MeV in EB, 300 MeV in EE). Electromagnetic "clusters" are thus formed, which in turn can be associated into "superclusters". The (super-)clustering algorithms are designed such as to collect in (super-)clusters a fraction as large and as stable as possible of the shower energy, in particular by recovering energy spread in ϕ due to secondary Bremsstrahlung emission and photon conversions in the material in front of the ECAL. On the other hand, they should also avoid collecting in the same (super-)cluster energy deposits due to different particles, and to minimize the effects of noise fluctuations.

For the Hybrid algorithm, a list of "seed" crystals with transverse energy above 1 GeV is first constructed. Starting from a seed crystal, a cluster is defined as an ensemble of ϕ-contiguous "dominos" which have collected an energy larger than 100 MeV. Each domino consists of 5 crystals with the same ϕ value, which corresponds to a domino width of 0.087 in η; if the central crystal energy is smaller than 1 GeV, only 3 crystals are used to form a domino (corresponding to a width of 0.053 in η). Valleys, where less than 100 MeV are collected in a domino, separate different clusters. The dominos are then clustered in ϕ, each distinct cluster of dominos being requested to have a seed domino with energy greater than 0.35 GeV. The ϕ roads are allowed to extend up to ± 10 crystals around the seed, which corresponds to ± 0.175 rad.

For the Island algorithm, the "seed" crystals are required to contain a transverse energy larger than 0.18 GeV. Starting from the most energetic seed, the Island algorithm collects energy deposits, first in the ϕ direction, then in η, until a rise in energy or a hole is found. Superclusters are built around the highest transverse energy cluster by connecting clusters in both directions. The road for superclustering is allowed to extend up to ± 0.2 rad in ϕ (i.e. ± 11 crystals) and ± 0.14 in η.

These algorithms thus differ slightly in the maximum ϕ extension for Bremsstrahlung recovery (± 10 crystals for the Hybrid algorithm versus ± 0.2 rad for the Island algorithm), and more significantly in the maximum lateral (η) extension of (super-)clusters. For both algorithms used in this analysis, an energy threshold of 4 GeV is requested for a supercluster.

[1)] It should be noted that the (super-)clustering algorithms and their parameters have been designed for energies much lower than in the present study, typically for electrons with $p_t \simeq 35$ GeV/c. The parameters have subsequently been tuned for low p_t electrons ($p_t \lesssim 10$ GeV/c) as described in [8, 10]. The parameters used for the present study are those defined in Refs. [3, 9].

3 Energy fraction $R_{\rm ECAL}$ measured in the ECAL

Figures 4(a) and (b) present, as a function of $|\eta|$, the energy fraction $R_{\rm ECAL}$ = $E_{\rm ECAL}$ / $E_{\rm true}$ of the electron initial energy collected in the most energetic ECAL supercluster, for 500 and 4000 GeV electrons, respectively. Note that in this Section and in the two following ones, saturation effects are not simulated; these effects are introduced in Section 7.

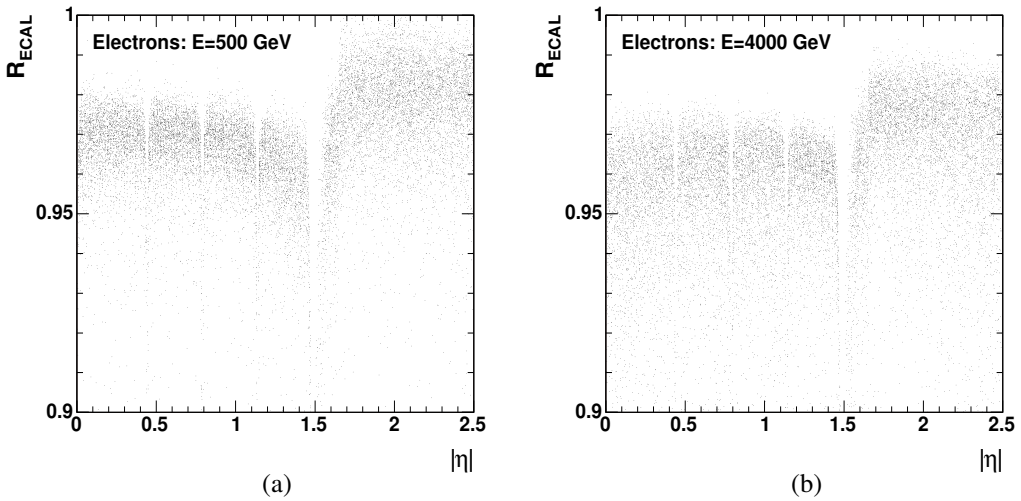

Figure 4: Distribution of $R_{\rm ECAL}$ = $E_{\rm ECAL}$ / $E_{\rm true}$ as a function of η for (a) 500 GeV and (b) 4000 GeV electrons (no electronics saturation effects are simulated).

In the vast majority of cases, more than 95% of the electromagnetic shower energy is measured in the ECAL, whereas gaps between modules and, most strikingly, between EB and EE, are visible as narrow η regions with lower energy collection.

However, the actual energy fraction measured in the ECAL depends both on η and on the initial particle energy. This is visible in Fig. 5 which presents, as a function of these two variables, the mean values of $R_{\rm ECAL}$ obtained from Gaussian fits to the measured distributions (it is recalled that the transition region between EB and EE is excluded from the analysis).

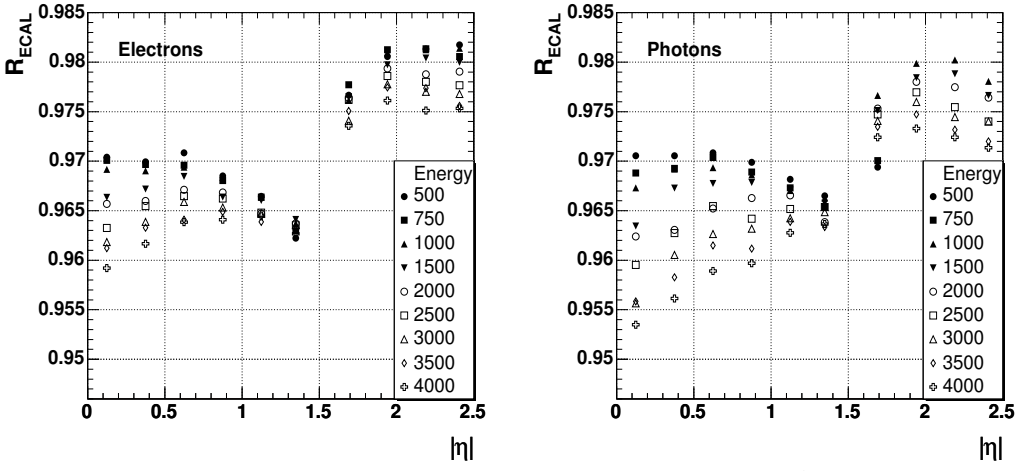

Figure 5: Mean value of $R_{\rm ECAL}$ as obtained from Gaussian fits, as a function of $|\eta|$ and of the incident particle energy for (a) electrons and (b) photons (no electronics saturation effects are simulated).

The energy collection in EE is higher by some 1% than in EB. In addition, an η dependence of the $R_{\rm ECAL}$ fraction is observed, which depends on energy: for 500 GeV electrons in the barrel, $R_{\rm ECAL}$ is highest for central rapidities,

and decreases at larger η values by up to 1%; for 4000 GeV electrons an effect of 0.5% in the other direction is observed. On the average, the energy fraction collected in the ECAL is $\sim 0.5\%$ higher for 500 GeV than for 4000 GeV electrons. Finally, the energy fraction collected in the ECAL is higher for electrons than for photons, mostly at highest energies and in the central η region.

These complex behaviours are the results of several physical effects, which are discussed in the next two Sections [2)].

4 Longitudinal shower containment and energy deposits in the HCAL

Good longitudinal containment of electromagnetic showers is provided by the CMS ECAL, with crystal lengths corresponding to $25.8\ X_0$ in EB and $(24.7 + 3)\ X_0$ in EE, taking the preshowers into account. Given the limited calorimeter depth, the longitudinal containment of high energy electron and photon showers depends critically on the initial particle energy, on shower length fluctuations and on the actual shower path in the ECAL, as will be shown in this Section.

4.1 Shower shape and length

The ECAL effective depth, averaged over ϕ, is slightly decreased by the presence of gaps between crystals and between modules, filled with air or with low density support material; this can be seen as a function of η in Fig. 6(a). On the other hand, crystal off-pointing is responsible for the increase of the effective calorimeter depth with $|\eta|$ (in addition to a small decrease of the effective calorimeter depth due to the ϕ off-pointing).

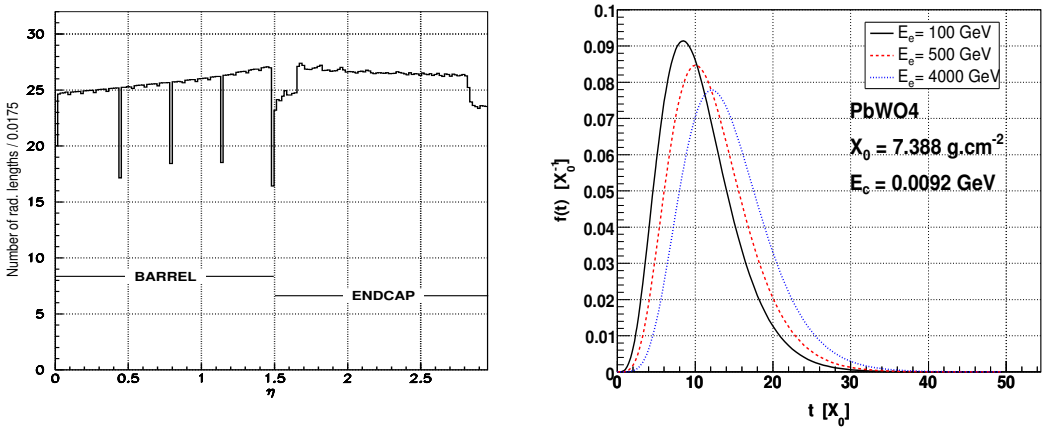

(a) (b)

Figure 6: (a) Effective ECAL depth, as a function of $|\eta|$ [7]. (b) Longitudinal distribution of the energy deposit, $f(t) = 1/E\ \mathrm{d}E/\mathrm{d}t$, as a function of the shower depth, t, expressed in units of X_0, for 100, 500 and 4000 GeV electrons, following the parameterisation of Ref. [11].

Shower lengths depend logarithmically on the energy. To study this effect, a standard electromagnetic shower parameterisation has been used [11]. Figure 6(b) presents the longitudinal distribution of the energy deposit as a function of the shower depth, expressed in units of X_0, for showers initiated by electrons of 100, 500 and 4000 GeV. The maximum of the energy deposit in showers initiated by 500 GeV electrons is 1.6 X_0 deeper than for 100 GeV showers; at 4000 GeV, this number is of 3.7 X_0. The fraction of the shower energy contained within given calorimeter depths, expressed in terms of X_0, is given in Table 1 for several incident electron energies.

The energy dependence of the longitudinal development thus explains that lower energy showers (500 GeV) are better contained than higher energy ones (4000 GeV), as observed in Fig. 5. The difference in collected energy fractions between barrel and endcaps can be attributed partly to the different effective calorimeter depths (in addition to the effect of the superclustering algorithms to be discussed in Section 5.1). As an example, for a crystal

[2)] For electron and photon energies below 100 GeV, the energy correction is performed according to the number of hit crystals (Ref. [3]). This procedure, however, is not suited for high energy showers and would lead to an overestimate of the incident particle energy of 2.5 to 3.5% in the barrel, where the Hybrid clustering algorithm is used, and of 3.5 to 4.5% in the endcap, where the Island algorithm is used.

X_0	25	26	27	28	29	30
500 GeV	98.3	98.7	99.1	99.3	99.5	99.7
1000 GeV	97.7	98.3	98.7	99.1	99.3	99.5
2000 GeV	97.0	97.7	98.3	98.8	99.1	99.3
4000 GeV	96.1	97.0	97.8	98.3	98.8	99.1

Table 1: Average fraction (in %) of the shower energy contained within given calorimeter depths expressed in terms of numbers of radiation lengths X_0, for several incident electron energies, following the parameterisation of Ref. [11].

length of 26 X_0 for the barrel and of 28 X_0 in the endcaps (25 X_0 for crystals + 3 X_0 for the preshowers), average shower containments of 98.2% and 99.0% are expected for 1000 GeV electrons, according to the parameterisation of Ref. [11] (see Table 1). The lower energy collection in the most external part of the endcaps ($|\eta| \lesssim 1.65$), visible in Fig. 4, can similarly be explained by the absence in this region of the $3X_0$ preshowers.

Shower length fluctuations have also to be taken into account. According to the parameterisation of Ref. [11], fluctuations for energies considered here correspond to about 1 X_0 in length or, equivalently, 1 X_0 modification of the effective calorimeter depth; it should be noted that effects of fluctuations in opposite directions – shorter or longer showers – do not cancel here, because they have asymmetric effects on the energy deposit.

The effective ECAL depth is also reduced for electrons entering into a gap and impacting on a side face instead of the front face of a crystal, as it is in the case of leakage of part of a shower in inter-module gaps.

Finally, differences appear between electrons and photons, as visible in Figure 5, because of different initial shower developments: the effective length of photon initiated showers is nearly 1 X_0 longer than for electrons [12].

4.2 Shower containment

High energy shower development also depends on the material budget in front of the calorimeter (tracker, supports, etc.), which corresponds to $0.35X_0$ to $1.4X_0$ (see Fig. 3(a)). As will be discussed in Section 5.2, this explains that, in spite of possible energy losses related to Bremsstrahlung emission and photon conversions, simulations including the description of the complete detector in front of the ECAL predict the collection of a larger energy fraction than for the case when this material is not included.

The sensitivity of the collected energy to the longitudinal shower containment was investigated by drastically changing the effective calorimeter depth, expressed in terms of the number of conversion lengths [3)]. This was performed by changing X_0 from 0.89 cm to 0.60 cm, i.e. multiplying the effective ECAL depth by a factor 1.5 and thus reducing longitudinal losses to a negligible amount ; the Moliere radius was not modified accordingly. Figure 7 shows that enforcing full longitudinal shower containment has a 0.6% effect for 500 GeV barrel electrons, and slightly less in the endcaps where the effective ECAL depth is slightly larger. The effect is much larger at 4000 GeV: 1.2% in the endcaps, and 1.6 to 2.3% in the barrel, depending on $|\eta|$ and thus on the ECAL depth. It is also worth noting (not shown) that the fluctuations of the measured energy fraction is – as expected – considerably reduced through this procedure.

Even with this much increased effective ECAL depth, the collected energy fraction does not reach 1.00. This is because of the lateral shower extension and algorithm effects discussed in Section 5, because of remaining gap and other geometrical effects, and possibly because of the step-like structure of the ECAL front face at large $|\eta|$ values.

4.3 Energy measurement in the HCAL

The incomplete containment of electromagnetic showers in the ECAL, especially at high energy, leads to the observation of energy deposits, $E_{\rm HCAL}$, measured in the hadronic calorimeter HCAL [4)]. This is shown in Fig. 8, which presents distributions of the electron or photon energy fraction $R_{\rm H/E}$ = $E_{\rm HCAL}$ / $E_{\rm ECAL}$ measured in the HCAL and ECAL calorimeters, for 1000 and 4000 GeV incident energies [5)]. Table 2 gives, for several electron

[3)] For practical reasons, the fast CMS detector simulation program FAMOS (version 132) [13] was used for this study. Results of the fast and full simulations are similar, and the small differences between them should not affect the present conclusions.

[4)] It should be noted that the energy measured in the HCAL is not calibrated to take into account the fact that the incoming particle is an electron and not a hadron.

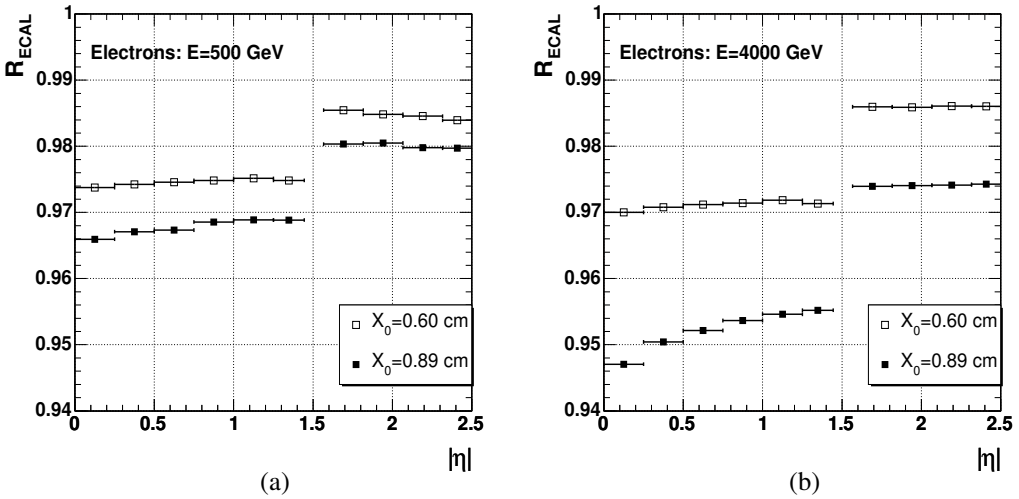

Figure 7: Energy fraction reconstructed in the ECAL, under the assumption that $X_0 = 0.89$ cm (as for $PbWO_4$ crystals, closed symbols), and $X_0 = 0.60$ cm (open symbols), for (a) 500 GeV and (b) 4000 GeV electrons (no electronics saturation effects are simulated) (FAMOS simulations).

energies, the fractions of showers with $R_{\mathrm{H/E}}$ larger than 0.01, 0.02, 0.05 and 0.10, and the average values of $R_{\mathrm{H/E}}$. As expected, the energy fraction measured in the HCAL increases significantly with the initial electron energy.

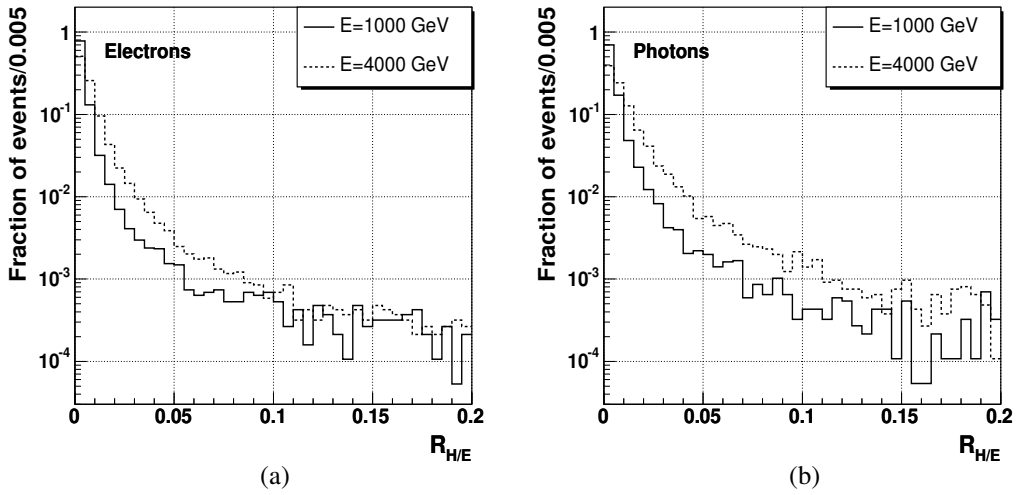

Figure 8: Distribution of $R_{\mathrm{H/E}}$ for 1000 and 4000 GeV electrons (a) and photons (b) (no electronics saturation effects are simulated).

An improved "measured energy" can thus be defined on an event by event basis, using the measured energy deposit in the HCAL: $E_{\mathrm{meas}} = E_{\mathrm{ECAL}} + E_{\mathrm{HCAL}} = E_{\mathrm{ECAL}} \cdot (1 + R_{\mathrm{H/E}})$. Figure 9 shows, as a function of $|\eta|$, the mean values of R_{ECAL} (closed symbols) and of R_{meas} = E_{meas} / E_{true} (open symbols); the means are determined from Gaussian fits to the distributions. The deficit of the measured energy compared to the true energy is reduced. However, dead material between the ECAL and the HCAL detectors corresponds to about 3 X_0 (see Fig. 3(b)); the energy measured in the HCAL is thus smaller than the full energy leakage from the ECAL.

In the barrel, the HCAL contribution is largest in the central rapidity region (0.2% for 500 GeV electrons up to 0.6% for 4000 GeV electrons), and becomes negligible for the largest $|\eta|$ values, where more tracker material is present and the effective ECAL depth is larger. For the endcaps, the HCAL correction is between 0.1% (500 GeV)

[5] To be precise, the energy ratio $R_{\mathrm{H/E}}$ is obtained using the energy measured in the HCAL cell situated beyond the seed of the ECAL supercluster, divided by the energy of the seed cluster.

$R_{\mathrm{H/E}} >$	0.01	0.02	0.05	0.10	$\langle R_{\mathrm{H/E}} \rangle$
500 GeV	6.3 %	2.9 %	1.5 %	0.8 %	0.006
1000 GeV	8.7 %	4.1 %	2.1 %	1.3 %	0.009
2000 GeV	12.9 %	5.8 %	2.5 %	1.6 %	0.012
4000 GeV	23.7 %	9.7 %	3.6 %	2.2 %	0.017

Table 2: Percentage of showers with $R_{\mathrm{H/E}}$ larger than 0.01, 0.02, 0.05 and 0.10 and average values of $R_{\mathrm{H/E}}$, for several electron energies (no electronics saturation effects are simulated).

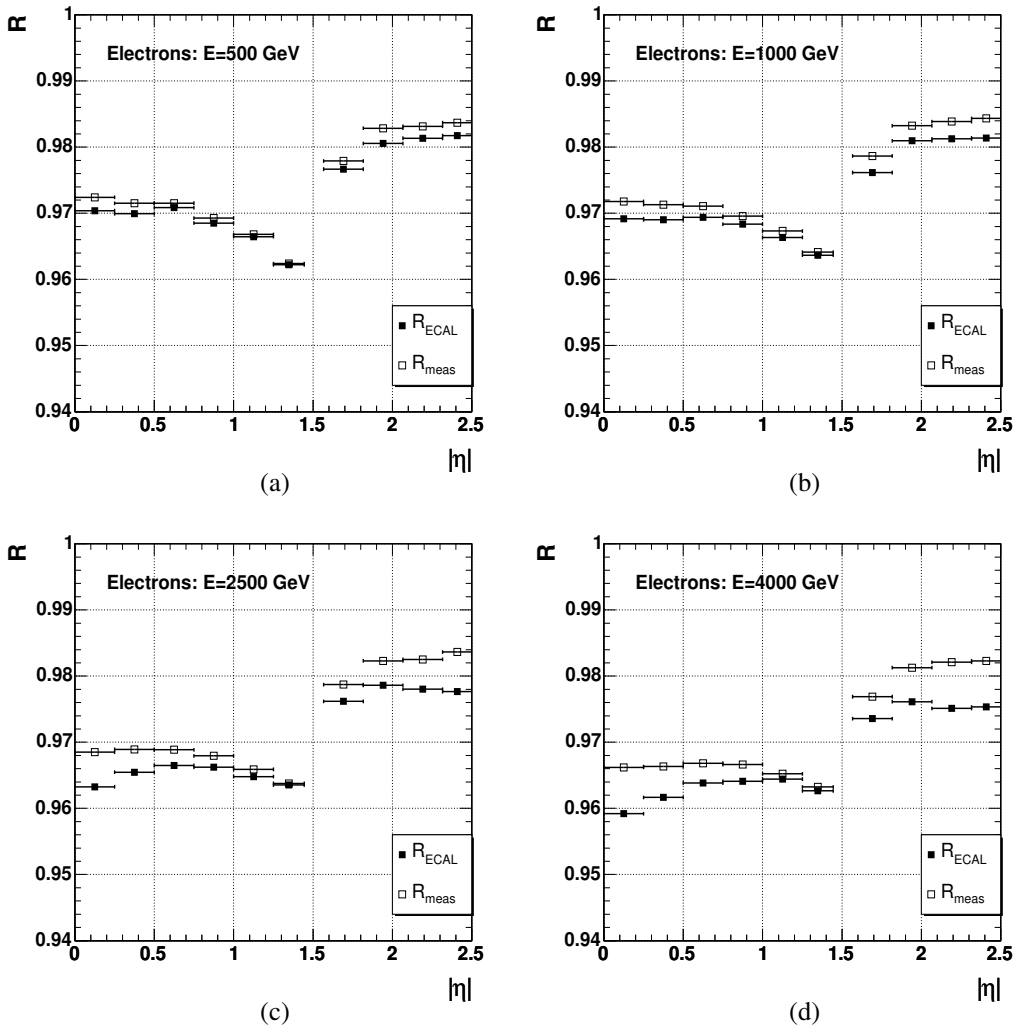

Figure 9: Mean values of R_{ECAL} (closed symbols) and R_{meas} (open symbols) as a function of $|\eta|$ for (a) 500, (b) 1000, (c) 2500 and (d) 4000 GeV electrons, as determined from Gaussian fits to the distributions (no electronics saturation effects are simulated).

and 0.4% (4000 GeV electrons) at the outer diameters (smaller EE $|\eta|$ values), where more material is present in front of the ECAL (but with imperfect preshower coverage for the most external, smallest $|\eta|$ region); it reaches 0.2% at 500 GeV and 0.7% at 4000 GeV for the region closer to the beam pipe (larger EE $|\eta|$ values).

5 Lateral shower extension and Bremsstrahlung effects

Additional energy losses can be due to the lateral shower extension, either in η due to definition of the superclustering algorithms, or in ϕ due to Bremsstrahlung and photon conversion effects. As will be seen in the present Section, these effects are relatively small in the present energy range.

5.1 (Super-)clustering effects

The crystal sizes and the (super-)clustering algorithms have been designed to ensure excellent lateral shower containment. As the crystal widths correspond approximately to one Moliere radius, only a small fraction of the shower energy is expected to leak outside the main (super-)cluster, even for the more restrictive "Hybrid" clustering algorithm applied in the EB, where the dominos have a maximal width in η of 5 crystals. However, a widening of the shower with energy and fluctuations in energy deposit can lead at high energy to losses related to the features of the (super-)cluster reconstruction algorithms. The lateral shower containment was thus studied by adding to the main supercluster energy that of additional "secondary" clusters, centered within a radius $\Delta R = \sqrt{\Delta\phi^2 + \Delta\eta^2} \leq 0.2$ around the shower center.

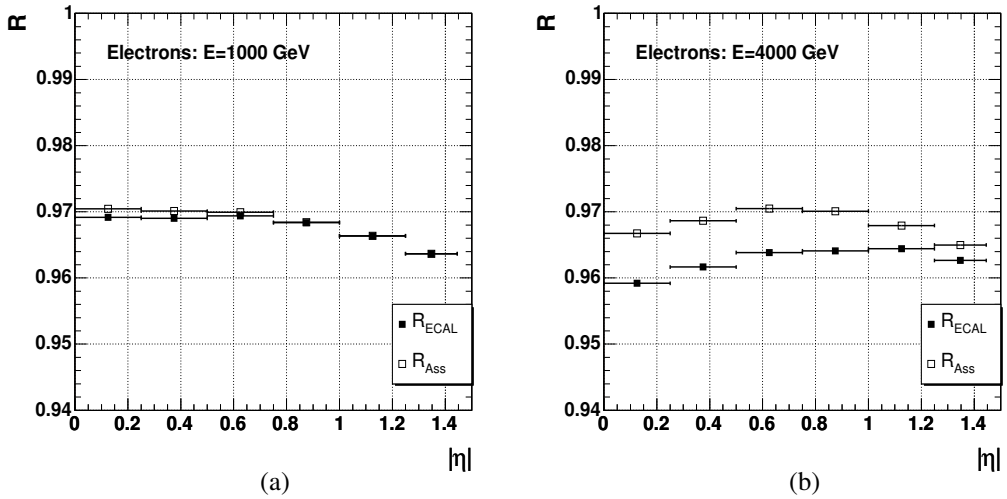

Figure 10: Energy fraction measured in the ECAL using the standard superclustering algorithms ($R_{\rm ECAL}$) and including "secondary" clusters reconstructed within a distance $\Delta R \leq 0.2$ of the shower center ($R_{\rm ass}$), for (a) 1000 and (b) 4000 GeV electrons (no electronics saturation effects are simulated).

In the barrel, the additional clusters have the same ϕ value as the shower center, and they increase slightly the shower extension in $|\eta|$. In the endcaps, where the Island algorithm can already extend up to $\Delta\eta = \pm 0.14$, no additional clusters are found. As seen in Fig. 10(a), the additional energy fraction collected with this extended range is of some 0.2% for $|\eta| \lesssim 0.5$, for 1000 GeV electrons. For 4000 GeV electrons, it is of 0.8% for $|\eta| \lesssim 0.5$, decreasing to 0.4% for $|\eta| \gtrsim 1.0$ (Fig. 10(b)).

5.2 Bremsstrahlung emission and photon conversions

As presented in Section 2.2, the (super-)clustering algorithms are designed to recover most of the energy spread in ϕ due to Bremsstrahlung emission and possible subsequent photon conversions in the material in front of the ECAL. In our case, remaining losses are expected to be small, in view of the small curvature of high energy tracks in the 4 T magnetic field of CMS: the purely geometrical distance between the impact point in the barrel of an electron with transverse energy of 500 GeV and that of a straight line is only 2 mm; it is less than 0.25 mm for electrons with transverse energy of 4000 GeV. Very large energy Bremsstrahlung emission leaving a low

momentum track, or subsequent photon conversions giving rise to electrons or positrons in the few GeV range, could however lead to losses in ϕ.

In order to study these effects, electron showers were simulated assuming no material in front of the ECAL, i.e. no beam pipe, no tracker detector and no service material.

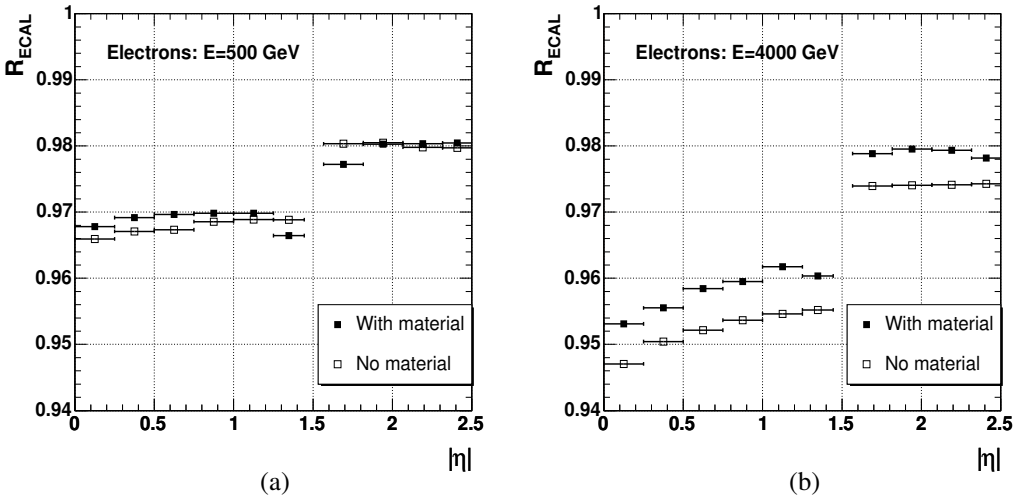

Figure 11: Mean values of $R_{\rm ECAL}$, as obtained from Gaussian fits to the distributions, as a function of $|\eta|$, for (a) 500 and (b) 4000 GeV electrons. The closed symbols are for the standard detector simulation and the open symbols for the case where no material is simulated in front of the ECAL (in both cases, no electronics saturation effects are simulated) (FAMOS simulations).

Figure 11 shows, as a function of $|\eta|$ and for electron energies of 500 and 4000 GeV, the mean values of $R_{\rm ECAL}$ as obtained from Gaussian fits to the distributions, for simulations with and without material in front of the ECAL. The measured energy fraction in the ECAL is not larger in the latter case, indicating that Bremsstrahlung emission and photon conversions in the material in front of the ECAL do not induce significant energy losses in the present energy range. On the contrary, especially at the highest energies, the presence of material in front of the ECAL helps collecting a larger energy fraction. This is attributed to an effective increase of the longitudinal shower containment in the ECAL due to the material in front of it. Indeed the effective calorimeter length is increased by the presence of additional material, while the non-measurement of the first shower fraction induces only a small reduction of the total energy collection (see Fig. 6(b)). For 500 GeV electrons, with rather well contained showers, the presence of dead material helps collecting 0.2% of the initial electron energy. In contrast, for 4000 GeV electrons, the presence of dead material in front of the ECAL has an overall effect of 0.5 to 0.7% to energy collection (see Fig. 11).

6 Energy and η dependent correction factors ($E \leq$ 2000 GeV in the barrel, $E \leq$ 4000 GeV in the endcaps)

In view of the numerous intricate effects discussed above, depending on energy, ϕ and η, the reconstruction of the initial particle energy can be obtained from the measured energy $E_{\rm meas} = E_{\rm ECAL} + E_{\rm HCAL}$, using energy and η dependent correction factors $F_{\rm cor}(E, \eta)$.

The purpose of the present Section is thus to determine these correction factors for electrons and photons with energies from 500 to 2000 GeV in the barrel and from 500 to 4000 GeV in the endcaps. For higher energies in the barrel, saturation effects have to be taken into account, which is the subject of Section 7.

For each sample, the $R_{\rm meas}$ = $E_{\rm meas}$ / $E_{\rm true}$ distribution is fitted according to a Gaussian law, and the inverse of the fit mean is taken as the correction factor $F_{\rm cor}(E, \eta)$. These factors are given in Table 3, both for electrons and for photons.

The distributions of the normalised reconstructed energy, after application of these correction factors, $R_{\rm cor} = F_{\rm cor} \times E_{\rm meas}/E_{\rm true}$, are presented in Fig. 12 for 500 and 2000 GeV electrons. The corrected distributions peak at

$\|\eta\|$	0. - 0.250	0.250 - 0.500	0.500 - 0.750	0.750 - 1.000	1.000 - 1.223	1.223 - 1.442	1.566 - 1.816	1.816 - 2.066	2.066 - 2.283	2.283 - 2.500
Electrons										
500 GeV	0.973	0.971	0.972	0.970	0.966	0.963	0.977	0.983	0.983	0.984
750 GeV	0.972	0.971	0.971	0.969	0.967	0.963	0.979	0.983	0.983	0.983
1000 GeV	0.972	0.971	0.971	0.970	0.967	0.964	0.979	0.983	0.984	0.984
1500 GeV	0.970	0.970	0.970	0.968	0.967	0.964	0.979	0.983	0.984	0.984
2000 GeV	0.970	0.969	0.970	0.968	0.966	0.964	0.978	0.983	0.984	0.984
2500 GeV	0.968	0.969	0.969	0.968	0.966	0.964	0.979	0.982	0.983	0.984
2500 GeV	*0.968*	*0.969*	*0.969*	*0.968*	*0.966*	*0.964*	0.979	0.982	0.983	0.984
3000 GeV	*0.967*	*0.968*	*0.969*	*0.967*	*0.966*	*0.964*	0.978	0.982	0.983	0.983
3500 GeV	*0.967*	*0.967*	*0.967*	*0.967*	*0.965*	*0.964*	0.978	0.982	0.982	0.983
4000 GeV	*0.966*	*0.966*	*0.967*	*0.967*	*0.965*	*0.963*	0.977	0.981	0.982	0.982
Photons										
500 GeV	0.973	0.972	0.972	0.971	0.969	0.967	0.973	0.983	0.984	0.982
750 GeV	0.972	0.972	0.972	0.970	0.968	0.966	0.974	0.983	0.984	0.982
1000 GeV	0.971	0.971	0.971	0.970	0.968	0.967	0.980	0.983	0.984	0.982
1500 GeV	0.969	0.970	0.970	0.969	0.968	0.966	0.979	0.982	0.983	0.981
2000 GeV	0.967	0.968	0.968	0.968	0.967	0.964	0.979	0.981	0.982	0.982
2500 GeV	*0.966*	*0.968*	*0.968*	*0.966*	*0.967*	*0.966*	0.978	0.982	0.982	0.982
3000 GeV	*0.963*	*0.966*	*0.966*	*0.965*	*0.966*	*0.965*	0.978	0.982	0.981	0.981
3500 GeV	*0.963*	*0.964*	*0.965*	*0.964*	*0.965*	*0.964*	0.977	0.981	0.981	0.981
4000 GeV	*0.962*	*0.962*	*0.963*	*0.963*	*0.964*	*0.964*	0.977	0.980	0.980	0.981

Table 3: Inverse of the energy and η dependent correction factors $F_{\rm cor}(E,\eta)$ for electrons and for photons with $E \leq 2000$ GeV in EB (i.e. below the saturation limit) and $E \leq 4000$ GeV in EE. The data in italics, for energies larger than 2000 GeV in the barrel, are computed without simulation of the saturation effects (see Section 7), and are given for information only.

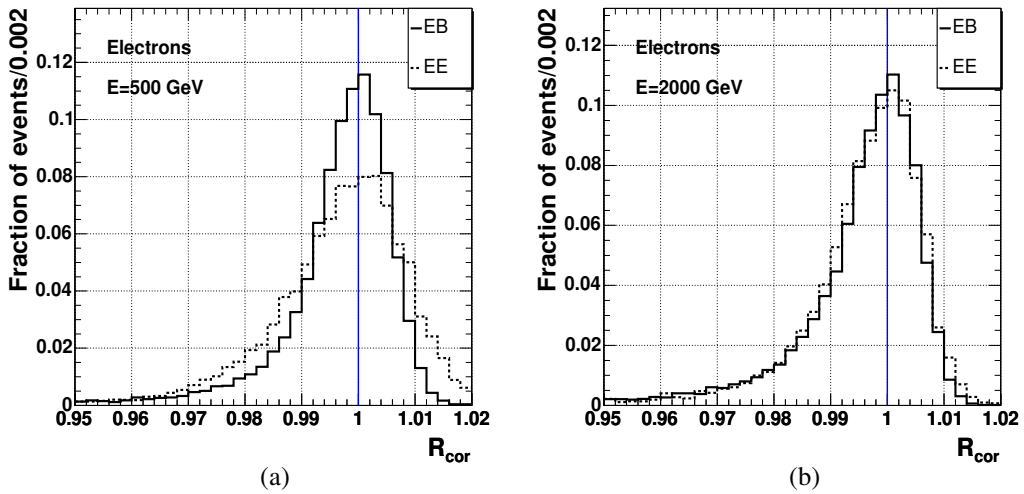

(a) (b)

Figure 12: Distribution of the normalised corrected energy $R_{\rm cor} = F_{\rm cor} \times E_{\rm meas} \ / \ E_{\rm true}$ for (a) 500 and (b) 2000 GeV electrons.

1.00 within less than 0.1% for all energy samples. Table 4 gives the average and the RMS values of $R_{\rm cor}$, as well as the mean (μ) and the standard deviation (σ) of Gaussian fits to the $R_{\rm cor}$ distributions. The error on the measured energy in the peak is of 0.6% in the barrel, and slightly higher in the endcaps.

Barrel								
	Electrons				Photons			
E (GeV)	average	RMS	μ	σ	average	RMS	μ	σ
500	0.9888	0.0470	1.0000	0.0054	0.9866	0.0500	0.9998	0.0055
750	0.9880	0.0509	0.9999	0.0053	0.9859	0.0526	0.9995	0.0060
1000	0.9868	0.0516	0.9999	0.0049	0.9843	0.0556	0.9994	0.0058
1500	0.9860	0.0536	1.0000	0.0051	0.9829	0.0554	0.9994	0.0058
2000	0.9858	0.0536	0.9997	0.0052	0.9823	0.0559	1.0000	0.0059
Endcaps								
	Electrons				Photons			
E (GeV)	average	RMS	μ	σ	average	RMS	μ	σ
500	0.9960	0.0182	1.0001	0.0082	0.9893	0.0429	1.0005	0.0082
750	0.9959	0.0185	0.9999	0.0070	0.9880	0.0436	1.0002	0.0058
1000	0.9957	0.0197	0.9999	0.0063	0.9946	0.0236	0.9999	0.0064
1500	0.9954	0.0192	0.9994	0.0060	0.9942	0.0220	0.9994	0.0069
2000	0.9948	0.0197	0.9996	0.0059	0.9933	0.0238	0.9989	0.0068

Table 4: Electron and photon energy resolution after correction (in the barrel and in the endcap separately): average and RMS of the normalised corrected energy distribution $R_{\rm cor}$ and mean (μ) and standard deviation (σ) of Gaussian fits.

7 Saturation and correction factors for $E > 2000$ GeV in the barrel

In case of a very high energy deposit in a single crystal, the readout electronics can saturate, as a consequence of the limited dynamical range of the multi-gain pre-amplifiers of the photomultipliers. Test beam studies have shown that saturation occurs in the barrel when the energy deposit in a single crystal exceeds 1700 GeV, and 3000 GeV in the endcaps [6] [4]. Because of the lateral shower extension over several crystals, saturation happens only for electrons or photons with energies larger than 2000 GeV; on the other hand, unsaturated events are still present at 4000 GeV, when the electron impact position is close to the edge of a crystal and the bulk of the energy is distributed over several crystals.

In the case of saturation, the energy deposit in the ECAL is not completely measured. A method based on the two-dimensional (η, ϕ) profile of the electromagnetic showers in the ECAL allows to correct for the loss of information due to saturation, using the energy deposits in the surrounding crystals [5].

In this Section, we first present further studies and improvements to the techniques presented in Ref. [5] (Section 7.1), and then determine energy correction factors in the energy range $E > 2000$ GeV (Section 7.2).

7.1 Saturation corrections

Following the method designed in Ref. [5], the E_1 – non-measured – energy deposit in a crystal with saturated electronics can be determined from the E_{24} energy deposit in the remaining 24 crystals of the 5×5 cluster surrounding the central, saturating crystal. The ratio E_1/E_{25} (with $E_{25} = E_1 + E_{24}$), however, depends on the impact position of the incident electron on the saturating crystal face: it is largest for a central impact, lower for impacts closer to the crystal edges. The energy distribution among the crystals of the 5×5 cluster is thus studied as a function of two variables, X and Y, which are related to the impact position. In Ref. [5], the variable X is defined as the logarithm of the ratio given by the sum of the energies collected in the 10 crystals of the 5×5 matrix with larger η values than the central crystal, divided by the sum of the energies of the 10 crystals with smaller η values. The variable Y is defined similarly, from the energy deposits in the 10 crystals with larger and smaller ϕ values than the central crystal. A correction function $F(X, Y)$ is then determined from simulation studies, to

[6] Given this high threshold, no saturation is simulated in this note for the endcaps.

reconstruct the unmeasured E_1 energy. It was found in Ref. [5] that this function has a negligible dependence in the incident energy.

In the following, we introduce slightly modified definitions of the X and Y variables, which take into account the left-right symmetry of the CMS detector around the nominal interaction point:

$$X = \ln(\frac{\Sigma_{\text{inner}}}{\Sigma_{\text{outer}}}), \tag{1}$$

where "inner" ("outer") refers to crystals with smaller (larger) pseudorapidity in *absolute* value $|\eta|$ than the central crystal;

$$Y = \ln(\frac{\Sigma_{\text{top}}}{\Sigma_{\text{bottom}}}) \quad (\eta > 0) \qquad Y = \ln(\frac{\Sigma_{\text{bottom}}}{\Sigma_{\text{top}}}) \quad (\eta < 0), \tag{2}$$

where "top" ("bottom") refers to crystals with larger (smaller) ϕ values than the central crystal.

The relevance of these modified definitions is due to the η and ϕ off-pointings of the ECAL crystals, as illustrated by Fig. 2(b): central impacts lead to larger energy deposits in "outer" crystals, and the present definition of X takes into account the mirror off-pointings of the crystals with $\eta < 0$ and $\eta > 0$. Similarly, the detector symmetry properties are taken into account for Y by the definitions of eq. 2.

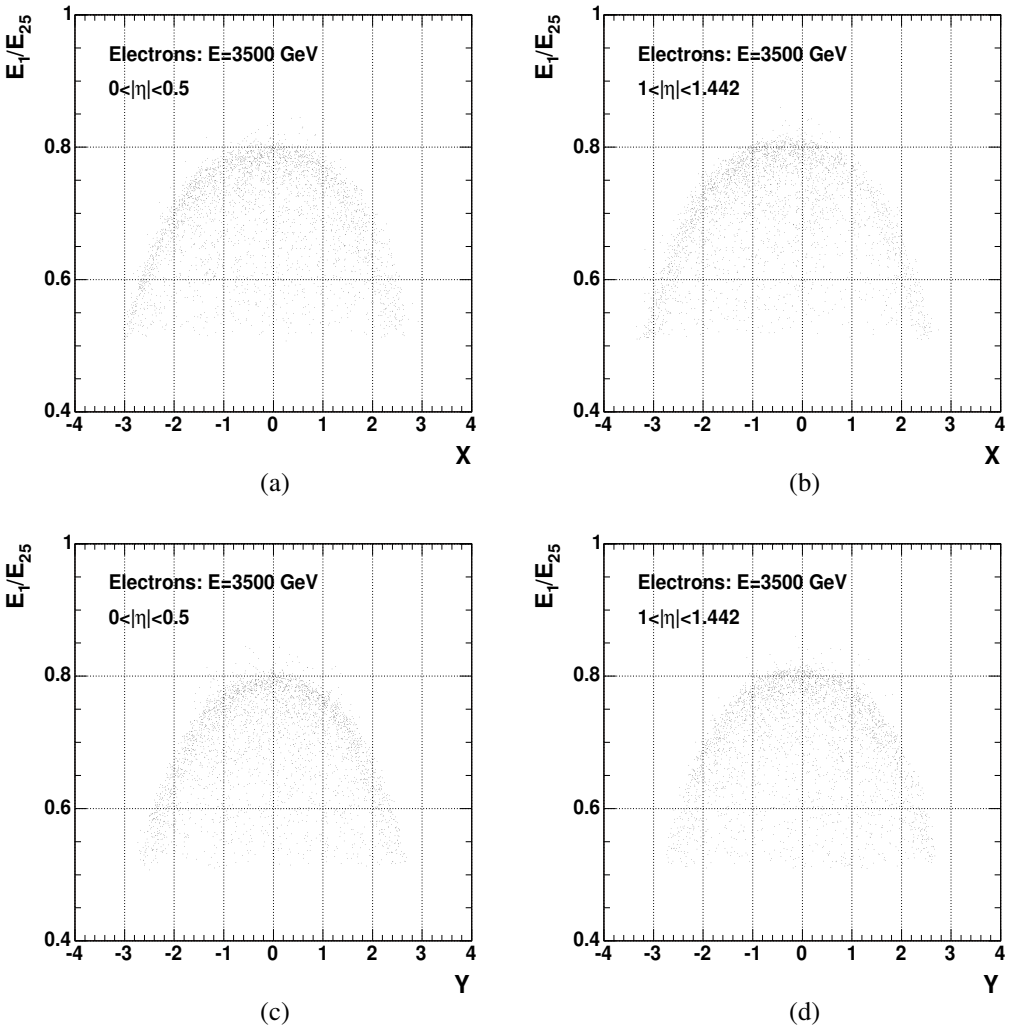

Figure 13: Distribution of the energy ratio E_1/E_{25} as a function of the variables X (Eq. 1, upper plots) and Y (Eq. 2, lower plots) for 3500 GeV incident electrons, in the cases where the energy deposit in the central crystal exceeds 1700 GeV (threshold for electronics saturation): (a, c) $|\eta| \leq 0.5$; (b, d) $1.0 < |\eta| \leq 1.442$.

Figure 13 presents the X and Y distributions for two $|\eta|$ ranges, as obtained for 3500 GeV incident electrons in the cases where the energy deposit in the central crystal exceeds 1700 GeV. As expected, the energy fraction in the

central crystal, E_1/E_{25}, decreases when the absolute value of X or Y increases, i.e. for non-central impacts, and the distributions are not symmetric around 0. This skewing is larger for X than for Y and the distributions present small but significant η dependences. No significant differences in the Y distributions are observed between e^- and e^+ simulated showers, indicating that magnetic field effects are unimportant in the present high energies.

The saturation correction function defined in Ref. [5] to describe the dependence of the E_1/E_{25} ratio into the X and Y variables is thus redefined here for three η ranges ($|\eta| \leq 0.5$, $0.5 < |\eta| \leq 1.0$ and $1.0 < |\eta| \leq 1.442$), and incorporates odd parity terms to describe the skewings in X and Y, in the form:

$$F(X,Y;\eta) = a \cdot (1 + bX + cX^2) \cdot e^{dX+eX^2} \cdot (1 + fY + gY^2) \cdot e^{hY+iY^2}. \quad (3)$$

The fitted form of the $F(X,Y;\eta)$ function for $|\eta| \leq 0.5$ is shown in Fig. 14(a). Figure 14(b) shows the distribution of the "residuals" defined as $[(E_1/E_{25}) - F(X,Y;\eta)]\ /\ (E_1/E_{25})$; it shows that the chosen function gives a satisfactory description of the data, the residuals being below a few % (the statistics in the large $|X|$, $|Y|$ bins are very low).

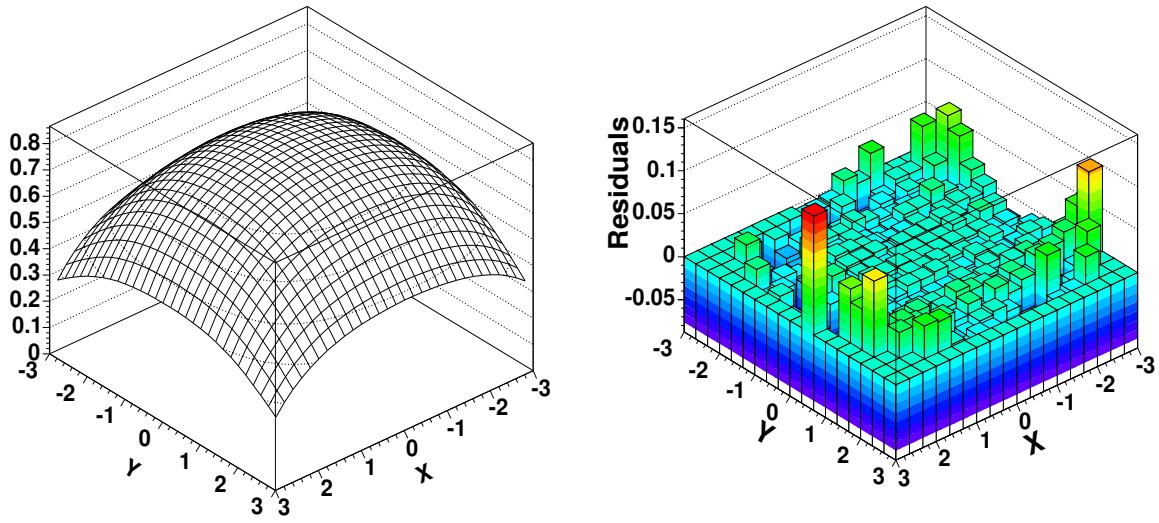

(a) (b)

Figure 14: (a) Fitted $F(X,Y;\eta)$ function (Eq. 3) describing the dependence of the E_1/E_{25} ratio into the X and Y variables, and (b) distribution of the residuals defined as $[(E_1/E_{25}) - F(X,Y;\eta)]\ /\ (E_1/E_{25})$, as a function of X and Y, for 3500 GeV incident electrons with $|\eta| \leq 0.5$, in the cases with electronics saturation (energy deposit in the central crystal larger than 1700 GeV).

Electrons									
η range	a	b	c	d	e	f	g	h	i
$0.0 < \|\eta\| \leq 0.5$	0.7959	-0.0197	-0.0624	0.0142	0.0376	0.0404	0.1059	-0.0380	-0.1334
$0.5 < \|\eta\| \leq 1.0$	0.7980	-0.0286	-0.0651	0.0192	0.0402	0.0218	0.1101	-0.0231	-0.1343
$1.0 < \|\eta\| \leq 1.422$	0.8005	-0.0374	-0.0641	0.0264	0.0400	0.0258	0.1057	-0.0263	-0.1290
Photons									
η range	a	b	c	d	e	f	g	h	i
$0.0 < \|\eta\| \leq 0.5$	0.8051	-0.0265	-0.0610	0.0261	0.0371	0.0521	0.1037	-0.0490	-0.1295
$0.5 < \|\eta\| \leq 1.0$	0.8038	-0.0269	-0.0650	0.0107	0.0404	0.0152	0.1413	-0.0148	-0.1576
$1.0 < \|\eta\| \leq 1.422$	0.8121	-0.0461	-0.0603	0.0350	0.0349	0.0220	0.1148	-0.0224	-0.1320

Table 5: Fitted parameters of the $F(X,Y;\eta)$ function (Eq. 3), for electrons and photons with electronics saturation, in three η ranges.

The fitted parameters are given in Table 5 for three η range. They were determined with 3500 GeV electrons, and apply well for energies from 2500 to 4000 GeV. As expected, the parameters $b - e$ related to the X distribution

show small correlation with the parameters $f - i$ related to the Y distribution, and strong anticorrelations are observed between pairs of parameters ($b - d$, $c - e$, etc.).

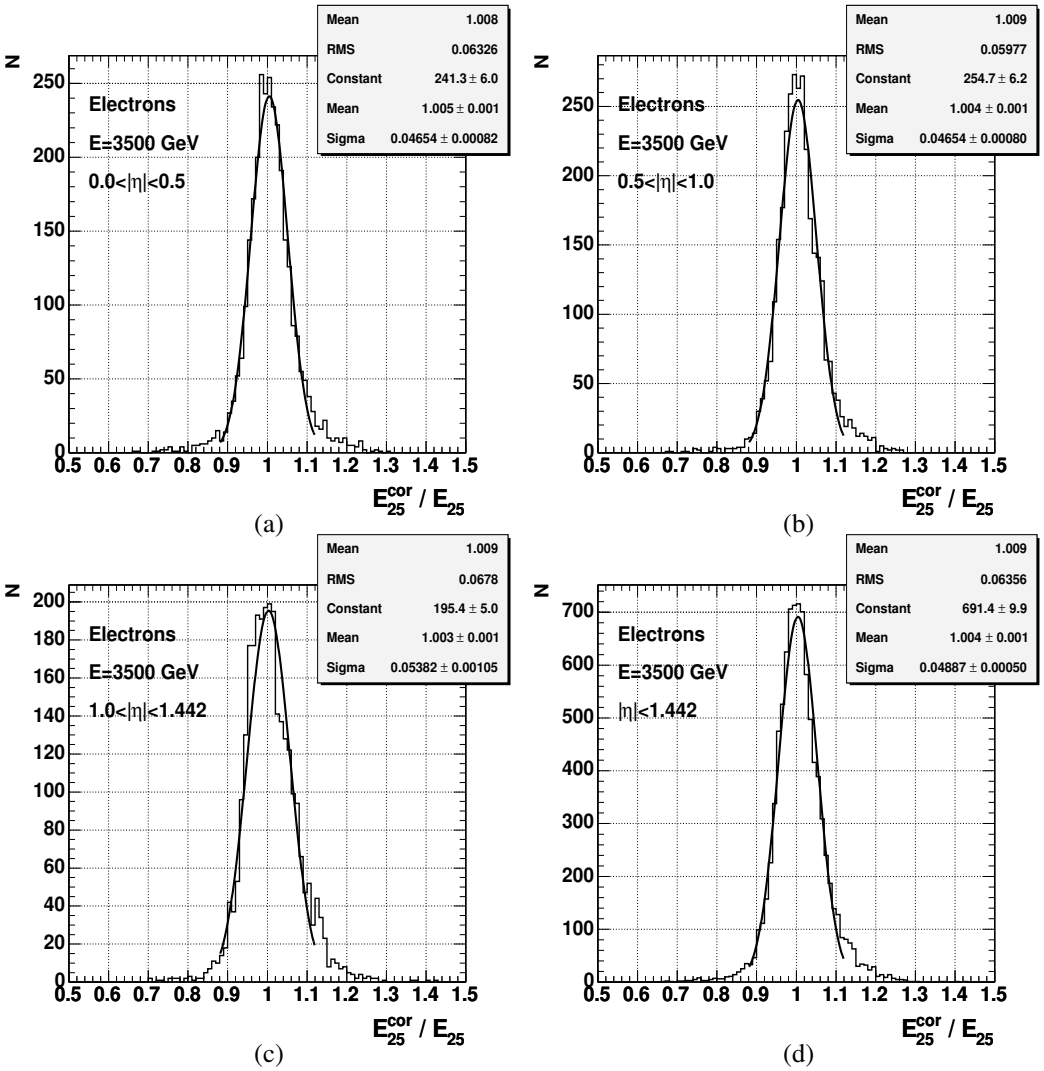

Figure 15: Distribution of the $E_{25}^{\rm cor}/E_{25}$ ratio for 3500 GeV electrons in the barrel with electronics saturation, for (a) $|\eta| \leq 0.5$, (b) $0.5 < |\eta| \leq 1.0$, (c) $1.0 < |\eta| \leq 1.442$ and (d) the whole barrel range $|\eta| \leq 1.442$.

Figure 15 shows the reconstructed $E_{25}^{\rm cor}$ energy divided by its nominal value E_{25}, for 3500 GeV electrons with electronics saturation, in three $|\eta|$ ranges and for the whole barrel. Table 6 gives the average and the RMS of the distributions, and the mean (μ) and the standard deviation (σ) of Gaussian fits, for electrons and photons of several incident energies with electronics saturation. The ratios peak at 1.00 and the resolution in the peak is of 5% on average for electrons and photons.

7.2 Energy and η dependent correction factors for $E > 2000$ GeV in the barrel

The determination of electron or photon energies larger than 2000 GeV in the barrel implies to correct first for possible saturation effects, and subsequently for the other effects discussed in the present note. For each energy sample, two sets of correction factors are thus determined, separately for "saturated" and "unsaturated" events.

For "unsaturated" events, where no crystal contains an energy deposit larger than 1700 GeV, correction factors are determined as in Section 6 and applied to the energy $E_{\rm meas}$, which includes ECAL and HCAL measurements.

For "saturated" events, where more than 1700 GeV are deposited in a single crystal, the $F(X, Y; \eta)$ saturation correction functions of Section 7.1 are first applied and, after adding the HCAL energy measurement (see section 4), the "measured" energy $E_{\rm meas}$ is determined. The latter is then used as in section 6 to determine correction factors $F_{\rm cor}(E, \eta)$ from Gaussian means of the $R_{\rm meas}$ = $E_{\rm meas}$ / $E_{\rm true}$ distributions.

	Electrons				Photons			
E (GeV)	average	RMS	μ	σ	average	RMS	μ	σ
2500	1.002	0.052	0.997	0.041	1.009	0.063	1.007	0.049
3000	1.005	0.061	1.000	0.046	1.005	0.069	1.004	0.055
3500	1.009	0.064	1.004	0.049	1.004	0.075	1.003	0.059
4000	1.012	0.070	1.005	0.053	1.006	0.084	1.003	0.063

Table 6: Resolution of the $E_{25}^{\rm cor}/E_{25}$ distributions in the cases with electronics saturation (energy deposits in the central crystal larger than 1700 GeV), after saturation correction using the fitted functions $F(X,Y;\eta)$ (Eq. 3) with the parameters given in Table 5: average and RMS of the distributions, and mean (μ) and standard deviation (σ) of Gaussian fits, for electrons and for photons.

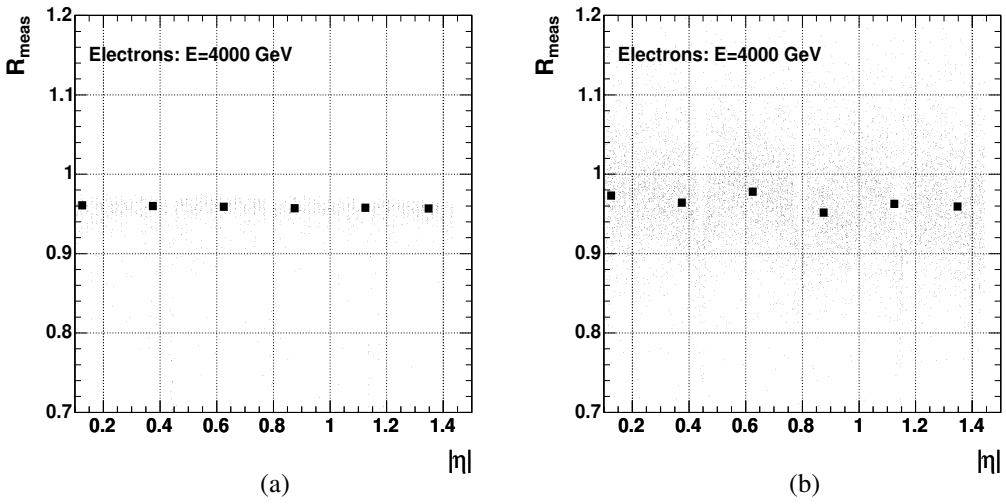

Figure 16: Distribution of $R_{\rm meas}$ = $E_{\rm meas}$ / $E_{\rm true}$, where $E_{\rm meas}$ includes ECAL and HCAL measurements, for 4000 GeV electrons in the barrel for (a) "unsaturated" and (b) "saturated" events; in the latter case, the ECAL energy includes saturation corrections. The closed symbols correspond to the mean values of Gaussian fits.

The distributions of $R_{\rm meas}$ are shown in Fig. 16 as a function of $|\eta|$ for 4000 GeV electrons, separately for "unsaturated" and for "saturated" events. The average values of $R_{\rm meas}$ are similar in both figures, but the dispersion is a factor 10 larger for "saturated" events, because of the uncertainty on the saturation correction: the resolution in the peak is $\simeq 0.6\%$ for unsaturated events (see Table 4) and $\simeq 5\%$ for saturated events (see Table 6).

The factors $F_{\rm cor}(E,\eta)$ are given in Table 7 for electrons and photons with $E > 2000$ GeV in the barrel.

8 Summary and conclusions

This note is devoted to a study of the expected response of the CMS electromagnetic calorimeter ECAL to high energy electrons and photons, from 500 to 4000 GeV, and the determination of energy and η dependent correction factors for improving the incident particle energy determination.

The energy reconstructed in the ECAL is some 2 to 4% lower than the incident particle energy, depending on the pseudo-rapidity η, on the particle energy, on whether the impact is in the barrel or in the endcaps (where the Hybrid and Island superclustering algorithms are used, respectively), and on the particle type (electrons or photons).

These losses are due to several effects, depending on the shower length and width, on the detector geometry, gaps and dead material between modules, and on the presence of dead material in front of the ECAL. The strongest effect is due to the longitudinal shower extension, which implies energy leakage beyond the ECAL; these losses are partly recovered in the hadronic calorimeter HCAL. In the barrel, when the Hybrid algorithm is used, small energy losses are also due to the lateral shower extension, increasing with energy. Bremsstrahlung and photon conversion effects do not induce significant energy losses.

$\|\eta\|$	0. - 0.250	0.250 - 0.500	0.500 - 0.750	0.750 - 1.000	1.000 - 1.223	1.223 - 1.442
Electrons, "unsaturated" events						
2500 GeV	0.967	0.967	0.967	0.966	0.964	0.962
3000 GeV	0.963	0.965	0.963	0.963	0.963	0.960
3500 GeV	0.959	0.962	0.962	0.962	0.961	0.958
4000 GeV	0.961	0.960	0.959	0.957	0.958	0.957
Photons, "unsaturated" events						
2500 GeV	0.964	0.966	0.967	0.965	0.965	0.964
3000 GeV	0.959	0.962	0.963	0.963	0.963	0.961
3500 GeV	0.956	0.960	0.960	0.961	0.960	0.957
4000 GeV	0.955	0.954	0.956	0.958	0.957	0.956
Electrons, "saturated" events						
2500 GeV	0.971	0.970	0.983	0.954	0.961	0.947
3000 GeV	0.972	0.969	0.975	0.961	0.965	0.951
3500 GeV	0.975	0.968	0.978	0.958	0.965	0.954
4000 GeV	0.973	0.964	0.978	0.952	0.963	0.959
Photons, "saturated" events						
2500 GeV	0.988	0.978	0.982	0.966	0.981	0.975
3000 GeV	0.988	0.971	0.979	0.952	0.984	0.971
3500 GeV	0.979	0.974	0.967	0.957	0.981	0.970
4000 GeV	0.966	0.965	0.962	0.943	0.983	0.971

Table 7: Inverse of the energy and η dependent correction factors $F_{\rm cor}(E,\eta)$ for electrons and photons in the barrel with $E > 2000$ GeV.

Energy and η dependent correction factors $F_{\rm cor}(E,\eta)$ have thus been determined, in order to reconstruct the incident particle energy using the signals measured in the ECAL and the HCAL.

In cases when electronics saturation occurs because more than 1700 GeV are deposited in a single crystal of the barrel, an improved technique has been designed to reconstruct the corresponding energy, using the measurements in the surrounding 5×5 crystal cluster. The specific energy correction factors $F_{\rm cor}(E,\eta)$ have been subsequently determined.

After correction, the distributions of the ratio of reconstructed over generated energies peak at 1.00, with a resolution in the peak of 0.6% in the case of no electronics saturation and 5% when saturation occurs.

References

[1] B. Clerbaux, T. Mahmoud, C. Collard and P. Miné, *Search with the CMS detector for heavy resonances decaying into an electron pair"*, **CMS NOTE 2006-083**.

[2] M.-C. Lemaire, V. Litvin and H. Newman, *Search for Randall-Sundrum excitations of gravitons decaying into two photons for CMS at LHC*, **CMS NOTE 2006-051**.

[3] CMS Collaboration, *The TriDAS Project technical Design Report, Volume II: Data Acquisition and High-Level Trigger"*, **CERN/LHCC 2002-026**, CMS TDR 6.2 (December 2002).

[4] M. Raymond, J. Crooks, M. French and G. Hall, *"The MGPA Electronic Calorimeter Readout Chip for CMS"*, Proceedings of the 2003 LECC Conference, **CERN-2003-006**.

[5] B. Clerbaux, T. Mahmoud, C. Collard, M.-C. Lemaire and V. Litvin, *"TeV electron and photon saturation studies"*, **CMS NOTE 2006-004**.

[6] OSCAR: CMS simulation Package Home Page, http://cmsdoc.cern.ch/oscar;
ORCA: CMS Reconstruction Package Home Page, http://cmsdoc.cern.ch/orca.

[7] CMS Collaboration, *"The Electromagnetic Calorimeter Project, Technical Design Report"*, **CERN/LHCC 1997-033**, CMS TDR 4 (December 1997).

[8] CMS Collaboration, *Physics Technical Design Report, Volume I: Detector performance and Software"*, **CERN/LHCC 2006-001**, CMS TDR 8.1 (February 2006).

[9] E. Meschi, T. Monteiro, C. Seez and P. Vikas, *"Electron Reconstruction in the CMS Electromagnetic Calorimeter"*, **CMS NOTE 2001-034**.

[10] S. Baffioni et al., *"Electron Reconstruction in CMS"*, **CMS NOTE 2006-040**.

[11] G. Grindhammer and S. Peters, *"The Parameterized Simulation of Electromagnetic Showers in Homogeneous and Sampling Calorimeters"*, hep-ex/0001020.

[12] W.-M. Yao et al., *Particle Data Group*, **J. Phys. G. 33**, 1 (2006).

[13] FAMOS: CMS Fast Simulation Package Home Page, http://cmsdoc.cern.ch/famos.